

Electrical spin protection and manipulation via gate-locked spin-orbit fields

Florian Dettwiler,¹ Jiyong Fu,^{2,*} Shawn Mack,^{3,†} Pirmin J. Weigele,¹
J. Carlos Egues,² David D. Awschalom,^{3,4} and Dominik M. Zumbühl^{1,‡}

¹Department of Physics, University of Basel, CH-4082, Basel, Switzerland

²Instituto de Física de São Carlos, Universidade de São Paulo, 13560-970 São Carlos, SP, Brazil

³Center for Spintronics and Quantum Computation,

University of California, Santa Barbara, California 93106, USA

⁴Institute for Molecular Engineering, University of Chicago, Chicago, IL 60637 USA

The spin-orbit (SO) interaction couples electron spin and momentum via a relativistic, effective magnetic field. While conveniently facilitating coherent spin manipulation^{1–3} in semiconductors, the SO interaction also inherently causes spin relaxation^{4–6}. A unique situation arises when the Rashba and Dresselhaus SO fields are matched^{7–9}, strongly protecting spins from relaxation, as recently demonstrated^{10,11}. Quantum computation and spintronics devices such as the paradigmatic spin transistor^{1,12} could vastly benefit if such spin protection could be expanded from a single point into a broad range accessible with *in-situ* gate-control, making possible tunable SO rotations under protection from relaxation.

Here, we demonstrate broad, independent control of all relevant SO fields in GaAs quantum wells, allowing us to tune the Rashba and Dresselhaus SO fields while keeping both *locked* to each other using gate voltages. Thus, we can electrically control and simultaneously protect the spin. Our experiments employ quantum interference corrections to electrical conductivity as a sensitive probe of SO coupling. Finally, we combine transport data with numerical SO simulations to precisely quantify all SO terms.

Spin-orbit coupling in a GaAs 2D electron gas (2DEG) has two dominant contributions: the Rashba¹³ and the Dresselhaus¹⁴ effects, arising from breaking of structural and crystal inversion symmetry, respectively. The Rashba coefficient α is proportional to the electric field in the quantum well (QW) and can be tuned with the doping profile¹⁰ as well as *in-situ* using gate voltages^{15,16}. We achieve independent control of α and carrier density n by using both top and back gates^{17,18}, at voltages V_T and V_B , respectively. To modify α at constant density, a change of V_T can be compensated by an appropriate change of V_B (see Fig. 1a), controlling α via a change of the gate-induced average electric field δE_Z , where $z \perp 2\text{DEG}$. Note that α can be continuously tuned to change sign.

The Dresselhaus term¹⁴, on the other hand, can be decomposed into sin/cos functions¹⁹ of θ (1st harmonic) and 3θ (3rd harmonic), with polar coordinate θ of the momentum \mathbf{k} in the 2DEG plane. The first harmonic has a coefficient $\beta = \beta_1 - \beta_3$ comprised of $\beta_1 = \gamma \langle k_z^2 \rangle$ and

9.3 nm QW, asymmetrically doped

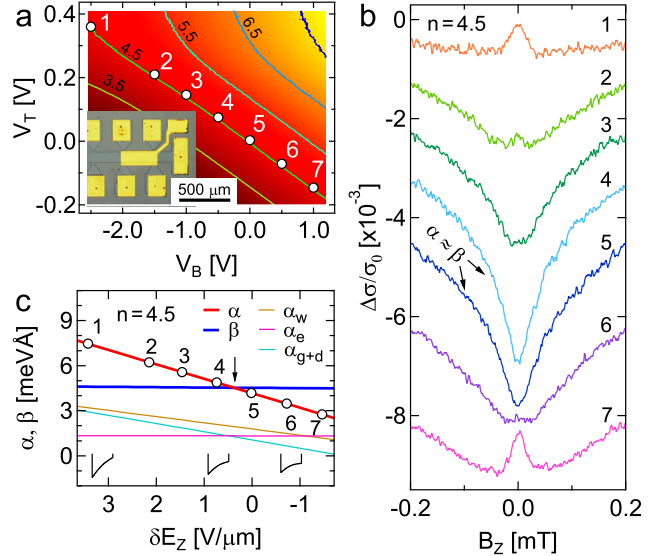


FIG. 1: **Weak localization (WL) as an $\alpha = \beta$ detector; gate-control of Rashba α at constant density.** **a** Measured charge density n (color) versus top gate voltage V_T and back gate voltage V_B (9.3 nm QW). Contours of constant density $3.5 - 7.5 \cdot 10^{11} \text{ cm}^{-2}$ are shown. Inset: optical micrograph of typical Hall bar, with contacts (yellow), gate (center) and mesa (black lines). **b** Normalized longitudinal conductivity $\Delta\sigma/\sigma_0 = (\sigma(B_Z) - \sigma(0))/\sigma(0)$ versus $B_Z \perp 2\text{DEG}$. Curves for gate configurations 1–7 along constant $n = 4.5 \cdot 10^{11} \text{ cm}^{-2}$ are shown (offset vertically), also labeled in panels **a** and **c**. **c** Simulated Rashba α and Dresselhaus β coefficients (see text) against gate-induced field change δE_Z , shown for constant $n = 4.5 \cdot 10^{11} \text{ cm}^{-2}$. The δE_Z axis – decreasing from left to right – corresponds exactly to the V_B abscissa of panel **a** for a covarying V_T such that $n = 4.5 \cdot 10^{11} \text{ cm}^{-2}$ constant. Sketches of the QW potential at 1, 4 and 6 illustrate the change of α with δE_Z . Note that $\alpha(\delta E_Z = 0) \neq 0$ since the external E-field (see SOM) is not zero at $\delta E_Z = 0$.

$\beta_3 = \gamma k_F^2/4$, where $k_F = \sqrt{2\pi n}$ is the Fermi wave number, $\gamma > 0$ is the bulk Dresselhaus parameter and $\langle k_z^2 \rangle$ depends on the width W of the well²⁰, with $\langle k_z^2 \rangle = (\pi/W)^2$ for infinite barriers. In addition, β_3 is the coefficient of the 3rd harmonic Dresselhaus term – hereafter cubic term – and depends on density n , thus enabling gate-control. The cubic term breaks the angular symmetry of the other terms and is relatively small compared to β_1 since $\langle k_z^2 \rangle \gg k_F^2/4$, except for the largest densities used.

To control β_1 , we studied QWs of widths $W = 8, 9.3, 11$ and 13 nm, yielding wave functions spreading over the full well width and $\langle k_z^2 \rangle < (\pi/W)^2$, see Fig. 2d, due to wave function penetration into the finite barriers. Over this range, β_1 changes by a factor 2 and is essentially independent of gate voltage.

Thus, we can set β_1 in discrete steps via QW width, and we achieve independent, continuous control of α and β_3 *in-situ* using top and back gates. This wide tunability makes it possible to change α while *locking* β to match α via gate-control of β_3 , thus strongly protecting spins from relaxation. In previous experiments, the Rashba and Dresselhaus fields were matched only at isolated points^{10,11,21}, not over a broad range. Finally, the broad gate-tunability gives us access to various SO regimes, such as the Dresselhaus (Rashba) regime $\beta \gg \alpha$ ($\alpha \gg \beta$), and allows a detailed characterization of the cubic term, which limits the spin lifetime even at $\alpha = \beta$.

Weak antilocalization (WAL) is a well established signature of SO coupling in magnetoconductance (MC) $\sigma(B_Z)$ ^{19,22–26}. For the $|\alpha| = \beta \gg \beta_3$ regime, the resulting internal SO magnetic field $\mathbf{B}_{\text{int}}(\mathbf{k})$ (see SOM) is uniaxial and vanishes for \mathbf{k} along one direction in the 2DEG plane (\hat{x}_- for $\beta = +\alpha$, or $\hat{x}_+(\perp\hat{x}_-)$ for $\beta = -\alpha$). Therefore, WAL (maximal $\sigma(B_Z = 0)$) is suppressed and the effectively spin-less situation exhibiting weak localization (WL) (minimal $\sigma(B_Z = 0)$) is restored^{7,8,21,24}. We introduce the SO lengths $\lambda_{\pm} = \hbar^2/(2m^*|\alpha \pm \beta|)$ (with Planck constant \hbar and effective mass m^*) as the *ballistic* length to be travelled along \hat{x}_{\pm} , respectively, for a spin rotation of one radian. For $\beta = +\alpha$, λ_- diverges (no precessions) while λ_+ is finite, and vice versa for $\beta = -\alpha$. We note that a closed-form theory of MC including all relevant SO terms is not currently available^{19,24–26}, making extraction of the SO parameters from MC difficult.

Figure 1b displays the MC of the 9.3 nm QW for configurations labeled 1–7, showing a transition from WAL (1 & 2) to WL (4 & 5) back to WAL (7) upon monotonically changing α on a contour of constant density, see Fig. 1a. Selecting the most pronounced WL curve allows us to determine the symmetry point $\alpha \approx \beta$. This scheme is repeated for a number of densities, yielding the symmetry point as a function of n . Thus, Rashba and Dresselhaus fields can be locked with gate voltages over a wide range (see Fig. 2a, blue markers), varying n by a factor of 2. Numerical simulations²⁷ (see methods) can accurately calculate α and $\langle k_z^2 \rangle$. This leaves only one fit parameter: γ , the bulk Dresselhaus coefficient, which can now be extracted from fits to the density dependence of the symmetry point, see solid blue line in Fig. 2a, giving excellent agreement. Further, the WL dip – often used to determine phase coherence – sensitively depends on the SO coupling (e.g. curves 3–6 in Fig. 1b), even before WAL appears. Negligence of SO coupling could thus lead to spurious or saturating coherence times.

Next, we change the Dresselhaus coefficient β_1 by varying the QW width and repeating the above procedure, summarized in Fig. 2a. For wider QWs, a smaller β_1 re-

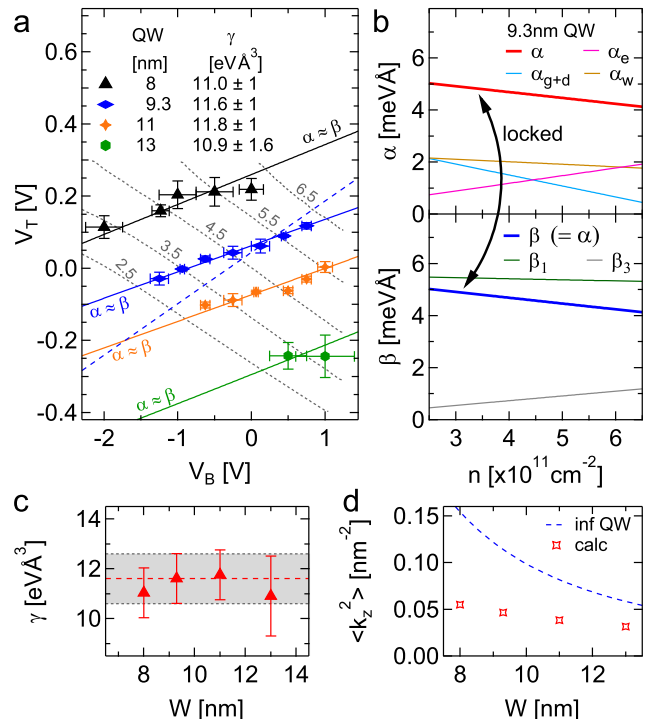


FIG. 2: **Tuning and locking** $\alpha = \beta$. **a** The markers indicate $\alpha \approx \beta$ for four different QW widths (asymmetric doping) and various densities (gray contours of constant n , labeled in units of 10^{11} cm^{-2}) in the V_B and V_T plane. Error bars result from the finite number of MC traces in the (V_B, V_T) -space. Theory fits (solid lines) are shown for each QW, with γ as the only fit parameter (inset table, error bars dominated by systematic error, see below). The dashed blue line indicates the slope of constant $\alpha = \beta_1$, neglecting β_3 , which is inconsistent with the data. **b** Simulation of locked $\alpha = \beta$ versus density n along solid blue line from **a**, showing the various SO contributions (see text). **c** Values of γ from fits to MC (red markers) and infinite (blue) potential. **d** $\langle k_z^2 \rangle$ as a function of QW width W for realistic (markers) and infinite (blue) potential.

sults, shifting the symmetry point towards smaller α , i.e. towards the lower right in Fig. 2a. As seen, locking of $\alpha = \beta$ is achieved in all present wavers. Further, reduced β_1 makes possible the Rashba regime $\alpha \gg \beta$, particularly in the upper left of Fig. 2a where α is large. Again performing fits over the density dependence of the symmetry point for each QW width, we obtain very good agreement, see Fig. 2a, and extract $\gamma = 11.6 \pm 1 \text{ eV \AA}^3$ consistently for all QWs (Fig. 2c). We emphasize that γ is notoriously difficult to calculate and measure^{25,26}; the value reported here agrees well with recent studies^{11,28,29}.

The Rashba coefficient is composed of $\alpha = \alpha_{\text{g+d}} + \alpha_{\text{w}} + \alpha_{\text{e}}$ in the simulation, with gate and doping term $\alpha_{\text{g+d}}$, QW structure term α_{w} , and Hartree term α_{e} . Along a contour of constant density, mainly $\alpha_{\text{g+d}}$ and α_{w} are modified, while α_{e} and β remain constant, see Fig. 1c.

11 nm QW, symmetrically doped

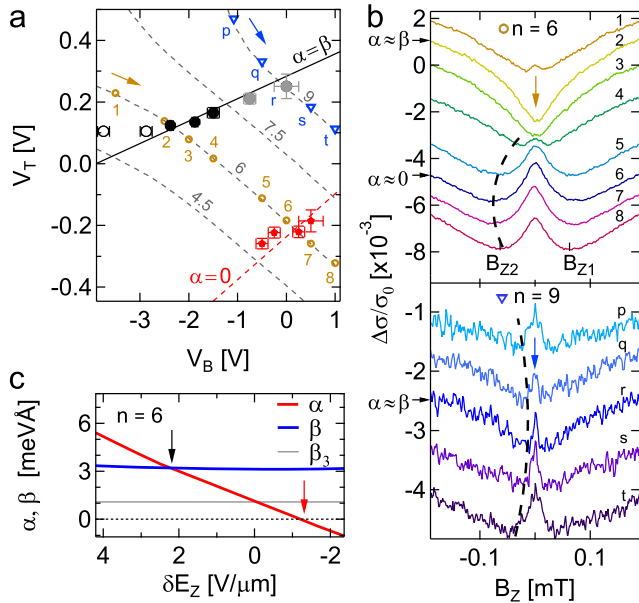


FIG. 3: The Dresselhaus and the cubic regime. **a** Locked regime $\alpha \approx \beta$ (black/grey symbols) and Dresselhaus regime $\alpha \approx 0$ (red symbols) from the broadest WAL minima (maximal B_{SO}) in the V_T and V_B plane for a more symmetrically doped 11 nm QW. The solid black line displays the $\alpha = \beta$ simulation, while the dashed red line marks the simulated $\alpha = 0$ contour. Open black markers (leftmost V_B) are entering the non-linear gate regime, causing a slight deviation from theory, which assumes linear gate action. The rightmost V_B points (gray) are obtained from the minimal B_{SO} in presence of WAL. **b** MC sequences at $n = 6 \cdot 10^{11} \text{ cm}^{-2}$ (upper panel) and $n = 9 \cdot 10^{11} \text{ cm}^{-2}$ (lower panel), shifted vertically for clarity. Each brown/blue marker in **a** corresponds to a trace in **b**, as labeled by numerals/letters. B_{SO} is indicated as a guide for the eye by black dashed curves for negative B_z . **upper panel** B_{SO} increases and peaks (indicating $\alpha = 0$) before decreasing again. **lower panel** broken spin symmetry regime: WAL is no longer suppressed here due to symmetry breaking from the cubic term at large n . Still, $\alpha \approx \beta$ can be identified with the narrowest WAL peak. **c** Simulation of α and β along $n = 6 \cdot 10^{11} \text{ cm}^{-2}$. α traverses both β (black arrow) and for smaller δE_z also zero (red arrow).

The density dependence for locked $\alpha = \beta$ (see Fig. 2b)) shows that while β_1 is nearly constant, β_3 is linearly increasing with n , thus reducing $\beta = \beta_1 - \beta_3$, and therefore forcing a corresponding reduction of α to keep $\alpha = \beta$ matched. The Hartree term α_e , however, increases for growing n . This is compensated by the other α -terms to nicely match $\beta(n)$, see Fig. 2b. Here, a change of $\sim 25\%$ in SO strength (~ 4 to $\sim 5 \text{ meV\AA}$) corresponds to a gate-controlled spin rotation of $\pi/2$ over a precession length of $5 \mu\text{m}$, which is clearly shorter than the spin diffusion length over the whole range, thus enjoying protection from spin relaxation.

We now show that α can be tuned through β and through zero in a more symmetrically doped wafer, opening the Dresselhaus regime $\beta \gg \alpha$. We introduce the

magnetic field B_{SO} where the MC exhibits minima at $B_{z1} \approx -B_{z2}$. Beyond the WAL-WL-WAL transition (Fig. 3b upper panel), B_{SO} is seen to peak and decrease again (dashed curve). The gate voltages with maximal B_{SO} are added to Fig. 3a for several densities (red markers). We surmise that these points mark $\alpha \approx 0$: B_{SO} signifies the crossover between WL/WAL-like MC, thus defining an empirical measure for the effects of SO coupling (larger B_{SO} , stronger effects). For $\alpha = 0$, the full effect of β on MC becomes apparent without cancellation from α , giving a maximal B_{SO} . Indeed, the simulated $\alpha = 0$ curve (dashed red line in Fig. 3a) cuts through the experimental points, also reflected in Fig. 3c by a good match with the simulated $\alpha = 0$ crossing point (red arrow).

For a comparison of experiment and simulation, we convert the empirical B_{SO} to a magnetic length $\lambda_{SO} = \sqrt{\hbar/2eB_{SO}}$, where $e > 0$ is the electron charge and the factor of two accounts for time-reversed pairs of closed trajectories. Fig. 4 shows the theoretical spin diffusion length λ_{eff} (see methods) and the ballistic λ_{\pm} , together with the experimental λ_{SO} , all agreeing remarkably well. First, we note that the ballistic λ_{\pm} and the diffusive λ_{eff} (small β_3) are equivalent. The enhanced λ_{SO} around $\alpha/\beta = 1$ corresponds to an increased spin relaxation time $\tau_{SO} = \lambda_{SO}^2/(2D)$. Second, $\max(\lambda_{\pm})$ quantifies the deviation from the *uniaxial* $\mathbf{B}_{\text{int}}(\mathbf{k})$ at $\alpha = \beta$ and thus the extent to which spin rotations are not undone in a closed trajectory due to the non-Abelian nature of spin rotations around non-collinear axes. This leads to WAL, a finite B_{SO} and $\lambda_{SO} \simeq \max(\lambda_{\pm})$, as observed (see Fig. 4). Unlike the corresponding time scales, the SO lengths are only weakly dependent on density and mobility when plotted against α/β , allowing a comparison of various densities.

The cubic term causes spin relaxation even at $\alpha = \beta$ and becomes visible at large densities: WAL is present in all traces and through $\alpha = \beta$ (Fig. 3b, lower panel), because $\mathbf{B}_{\text{int}}(\mathbf{k})$ can no longer be made uniaxial, thus breaking spin symmetry and reviving WAL. A partial symmetry restoration is still apparent, where – in contrast to the $\alpha = 0$ case – a *minimal* B_{SO} is reached (dashed curves) consistent with $\alpha = \beta$ (grey markers Fig. 3a at large n). We include the cubic β_3 in the spin relaxation time τ_{eff} (see methods), shown in the inset of Fig. 4 for two densities, finding good agreement with the experimental $\tau_{SO} = \lambda_{SO}^2/(2D)$, where D is the diffusion constant. Over the whole locked regime of Fig. 2b, WAL is absent, and τ_{SO} is enhanced between one and two orders of magnitude compared to $\alpha = 0$. Finally, the coherence length L_{φ} sets an upper limit for the visibility of SO effects: WAL is suppressed for $\lambda_{\text{eff}} \gg L_{\varphi}$, setting the width of the WAL-WL-WAL transition (see SOM).

As an outlook, this work is laying the foundation for a new generation of experiments benefiting from unprecedented command over SO coupling in semiconductor nanostructures such quantum wires, quantum dots, and electron spin qubits. We note that analogous SO

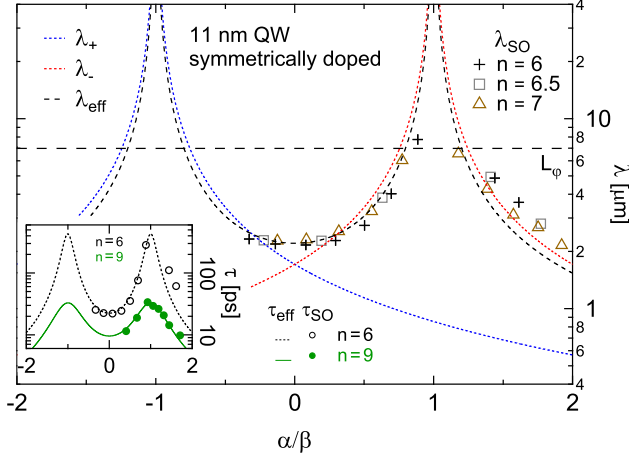


FIG. 4: **Experimental and theoretical SO-lengths and SO-times.** Experimental $\lambda_{\text{SO}} = \sqrt{\hbar/2eB_{\text{SO}}}$ (markers, densities as labeled, in units of 10^{11} cm^{-2}) as a function of the dimensionless ratio α/β (from SO simulation). The ballistic λ_{\pm} (blue/red dashes) and effective λ_{eff} (black dashed curve) are only weakly n -dependent (small β_3) when plotted against α/β . Thus, curves for only one density ($n = 6 \cdot 10^{11} \text{ cm}^{-2}$) are shown. The experimental uncertainty on λ_{SO} is captured by the spread given by the three slightly different densities. The coherence length $L_\varphi \approx 7 \mu\text{m}$ is added for illustration (obtained from WL curves), setting the visibility of SO effects in MC and thus the width of the WAL-WL-WAL transition. Inset: experimental spin relaxation time $\tau_{\text{SO}} = \lambda_{\text{SO}}^2/(2D)$ (circles) as a function of α/β for two densities as indicated. Theory curves τ_{eff} (dashed) now include the symmetry breaking third harmonic term, preventing divergence at $\alpha/\beta = 1$, while λ_{eff} (main panel) does not.

control is in principle also possible in other semiconductors. Finally, SO coupling is crucial beyond spintronics and quantum computation, e.g. for novel states of matter such as helical states, topological insulators, Majorana fermions and parafermions.

Materials and Methods

GaAs QW materials. The QWs are grown on an n -doped substrate (for details see SOM) and fabricated into Hall bar structures (see inset, Fig. 1a) using standard photolithographic methods. The 2DEG is contacted by thermally annealed GeAu/Pt Ohmic contacts, optimized for a low 2DEG contact resistance while maintaining high back gate tunability (low leakage currents) and avoiding short circuits to the back gate. On one segment of the Hall bar, a Ti/Au top gate with dimensions of $300 \times 100 \mu\text{m}^2$ was deposited. The average gate-induced E-field change in the QW is defined as $\delta E_Z = 1/2 (V_T/d_T - V_B/d_B)$, with effective distance $d_{T/B}$ from the QW to the top/back gate, extracted using a capacitor model, consistent with the full quantum description (see SOM). Contours of constant density follow $\delta V_T/d_T = -\delta V_B/d_B$. Deviations from linear behavior appear at most positive/negative gate voltages due to incipient gate leakage and hysteresis.

Low temperature electronic measurements. The experiments are performed in a dilution refrigerator with base temperature 20 mK. We have used a standard four-wire lock-

in technique at 133 Hz and 100 nA current bias, chosen to avoid self-heating while maximising the signal. The density is determined with Hall measurements in the classical regime, whereas Shubnikov-de Haas oscillations were used to exclude occupation of the second subband, which is the case for all the data discussed. The WAL signature of MC is a small correction (10^{-3}) to total conductance. To achieve a satisfactory signal-to-noise ratio, longitudinal conductivity traces $\Delta\sigma/\sigma_0 = (\sigma(B) - \sigma(0))/\sigma(0)$ were measured at least 10 times and averaged.

Numerical Simulations. The simulations calculate the Rashba coefficient α and $\langle k_z^2 \rangle$ based on the bulk semiconductor band parameters, the QW structure, the measured QW electron densities and the measured gate lever arms. We solve the Schrödinger and Poisson equations self-consistently (“Hartree approximation”), obtain the self-consistent eigenfunctions, and then determine α via appropriate expectation values²⁷. The Dresselhaus coefficient γ is extracted from fits of the simulation to the experiment which detects the absence of WAL at $\alpha = \beta = \gamma(\langle k_z^2 \rangle - k_F^2/4)$. Thus, given α and $\langle k_z^2 \rangle$ from the simulation and the measured $n = k_F^2/(2\pi)$, we obtain $\gamma = 11.6 \pm 1 \text{ eV}\text{\AA}^3$ consistently for all asymmetrically doped QWs. Taking into account the uncertainties of the band parameters, the experimental errors and a negligible uncertainty on $\langle k_z^2 \rangle$, an overall uncertainty of about 9–10% or about $\pm 1 \text{ eV}\text{\AA}^3$ on γ results. About 1–2% error originates from the experimental uncertainty of determining $\alpha = \beta$. The doping distribution (above/below QW) is not expected to influence γ , and hence we use the same γ for the more symmetrically doped wafer. Fits to the $\alpha = \beta$ experimental points then determine how much charge effectively comes from upper rather than lower doping layers, fixing the last unknown parameter also for the more symmetrically doped QW (see SOM).

Spin-dephasing times and lengths. In WL/WAL measurements, additional spin dephasing is introduced by the external magnetic field B via the Aharonov-Bohm phase arising from the magnetic flux enclosed by the time reversed trajectories: $\Delta\varphi = 2eAB/\hbar$, where A is the loop area. Here we take $A = \lambda_{\text{SO}}^2 = 2D\tau_{\text{SO}}$ as a characteristic “diffusion area” probed by our WL/WAL experiment, with τ_{SO} being the spin dephasing time, and λ_{SO} the spin diffusion length. By taking $\Delta\varphi = 1$ (rad) at $B = B_{\text{SO}}$, we can extract τ_{SO} from the minima of the WAL curves, which yields $\tau_{\text{SO}} = \hbar(4eDB_{\text{SO}})^{-1}$. The factor of 4 here stems from the two time-reversed paths and the diffusion length.

Effective SO times and lengths. Theoretically, we determine τ_{SO} via a spin random walk process (D’yakonov-Perel (DP)). The initial electron spin in a loop can point (with equal probability) along the s_{x-} , s_{x+} , and s_z axes (analogous to x_+ , x_- , and z , respectively), which have unequal spin-dephasing times $\tau_{\text{DP},s_{x-}}$, $\tau_{\text{DP},s_{x+}}$, and τ_{DP,s_z} . Hence, for unpolarized, independent spins, we take the average $\tau_{\text{eff}} = (\tau_{\text{DP},s_{x-}} + \tau_{\text{DP},s_{x+}} + \tau_{\text{DP},s_z})/3$ which leads to an average spin dephasing length $\lambda_{\text{eff}} = \sqrt{2D\tau_{\text{eff}}}$. In the SOM, we discuss the spin random walk and provide expressions for the DP times including corrections due to the cubic β_3 term. Figure 4 shows curves for the spin dephasing times and lengths presented here. In the main panel, the cubic β_3 is neglected in λ_{eff} since for $n \leq 7 \cdot 10^{11} \text{ cm}^{-2}$, WL appears at $\alpha = \beta$ (small β_3). In contrast, the cubic term is included in τ_{eff} in the inset since at the higher density $n = 9 \cdot 10^{11} \text{ cm}^{-2}$, WAL persists (strong β_3).

- * Permanent address: Department of Physics, Qufu Normal University, Qufu, Shandong, 273165, China
- † Current address: Naval Research Laboratory, Washington, DC 20375, USA
- ‡ Electronic address: dominik.zumbuhl@unibas.ch
- ¹ Datta, S. & Das, B. Electronic analog of the electro-optic modulator. *Applied Physics Letters* **56**, 665 (1990).
 - ² Golovach, V. N., Borhani, M. & Loss, D. Electric-dipole-induced spin resonance in quantum dots. *Physical Review B* **74**, 165319 (2006).
 - ³ Nowack, K. C., Koppens, F. H. L., Nazarov, Y. V. & Vandersypen, L. M. K. Coherent control of a single electron spin with electric fields. *Science* **318**, 1430 (2007).
 - ⁴ Golovach, V. N., Khaetskii, A. & Loss, D. Phonon-induced decay of the electron spin in quantum dots. *Physical Review Letters* **93**, 016601 (2004).
 - ⁵ Kroutvar, M. *et al.* Optically programmable electron spin memory using semiconductor quantum dots. *Nature* **432**, 81 (2004).
 - ⁶ Amasha, S. *et al.* Electrical control of spin relaxation in a quantum dot. *Physical Review Letters* **100**, 046803 (2008).
 - ⁷ Schliemann, J., Egues, J. C. & Loss, D. Nonballistic spin-field-effect transistor. *Physical Review Letters* **90**, 085323 (2003).
 - ⁸ Bernevig, B., Orenstein, J. & Zhang, S.-C. Exact SU(2) symmetry and persistent spin helix in a spin-orbit coupled system. *Physical Review Letters* **97**, 236601 (2006).
 - ⁹ Duckheim, M., Maslov, D. L. & Loss, D. Dynamic spin-hall effect and driven spin helix for linear spin-orbit interactions. *Physical Review B* **80**, 235327 (2009).
 - ¹⁰ Koralek, J. D. *et al.* Emergence of the persistent spin helix in semiconductor quantum wells. *Nature* **458**, 610 (2009).
 - ¹¹ Walser, M. P., Reichl, C., Wegscheider, W. & Salis, G. Direct mapping of the formation of a persistent spin helix. *Nature Physics* **8**, 757 (2012).
 - ¹² Koo, H. C. *et al.* Control of spin precession in a spin-injected field effect transistor. *Science* **325**, 1515 (2009).
 - ¹³ Bychkov, Y. A. & Rashba, E. I. Properties of a 2d electron gas with lifted spectral degeneracy. *JETP Letters* **39**, 78 (1984).
 - ¹⁴ Dresselhaus, G. Spin-orbit coupling effects in zinc blende structures. *Physical Review* **100**, 580 (1955).
 - ¹⁵ Engels, G., Lange, J., Schäpers, T. & Lüth, H. Experimental and theoretical approach to spin splitting in modulation-doped $\text{In}_x\text{Ga}_{(1-x)}\text{As}/\text{InP}$ quantum wells for $b \rightarrow 0$. *Physical Review B* **55**, R1958 (1997).
 - ¹⁶ Nitta, J., Akazaki, T., Takayanagi, H. & Enoki, T. Gate control of spin-orbit interaction in an inverted $\text{In}_{0.53}\text{Ga}_{0.47}\text{As}/\text{In}_{0.52}\text{Al}_{0.48}\text{As}$ heterostructure. *Physical Review Letters* **78**, 1335 (1997).
 - ¹⁷ Papadakis, S. J., De Poortere, E. P., Manoharan, H. C., Shayegan, M. & Winkler, R. The effect of spin splitting on the metallic behavior of a two-dimensional system. *Science* **283**, 2056 (1999).
 - ¹⁸ Grundler, D. Large Rashba splitting in InAs quantum wells due to electron wave function penetration into the barrier layers. *Physical Review Letters* **84**, 6074 (2000).
 - ¹⁹ Iordanskii, S. V., Lyanda-Geller, Y. B. & Pikus, G. E. Weak localization in quantum wells with spin-orbit interaction. *JETP Letters* **60**, 206 (1994).
 - ²⁰ Luo, J., Munekata, H., Fang, F. F. & Stiles, P. J. Effects of inversion asymmetries on electron energy band structures in GaSb/InAs/GaSb quantum wells. *Physical Review B* **41**, 7685 (1990).
 - ²¹ Kohda, M. *et al.* Gate-controlled persistent spin helix state in (In, Ga) As quantum wells. *Physical Review B* **86**, 081306 (2012).
 - ²² Bergmann, G. Weak localization in thin films: a time-of-flight experiment with conduction electrons. *Physics Reports* **107**, 1 (1984).
 - ²³ Altschuler, B. L. & Aronov, A. G. Electron-electron interactions in disordered conductors. *Electron-Electron Interactions in Disordered Systems*, Edited by A. L. Efros and M. Pollak (1985).
 - ²⁴ Pikus, F. G. & Pikus, G. E. Conduction-band spin splitting and negative magnetoresistance in A_3B_5 heterostructures. *Physical Review B* **51**, 16928 (1995).
 - ²⁵ Knap, W. *et al.* Weak antilocalization and spin precession in quantum wells. *Physical Review B* **53**, 3912 (1996).
 - ²⁶ Miller, J. B. *et al.* Gate-controlled spin-orbit quantum interference effects in lateral transport. *Physical Review Letters* **90**, 076807 (2003).
 - ²⁷ Calsaverini, R. S., Bernardes, E., Egues, J. C. & Loss, D. Intersubband-induced spin-orbit interaction in quantum wells. *Physical Review B* **78**, 155313 (2008).
 - ²⁸ Krich, J. & Halperin, B. Cubic Dresselhaus spin-orbit coupling in 2D electron quantum dots. *Physical Review Letters* **98**, 226802 (2007).
 - ²⁹ Walser, M. P. *et al.* Dependence of the Dresselhaus spin-orbit interaction on the quantum well width. *Physical Review B* **86**, 195309 (2012).

I. ACKNOWLEDGMENTS

We would like to thank A. C. Gossard, D. Loss, D. L. Maslov, G. Salis for valuable inputs and stimulating discussions. This work was supported by the Swiss Nanoscience Institute (SNI), NCCR QSIT, Swiss NSF, ERC starting grant, EU-FP7 SOLID and MICROKELVIN, US NSF and ONR, Brazilian grants FAPESP, CNPq, PRP/USP (Q-NANO), and natural science foundation of China (Grant No. 11004120).